Battery Electrodes, Electrolytes, and Their Interfaces

Iek-Heng Chu, Minghao Zhang, Shyue Ping Ong, and Ying Shirley Meng

Contents

Abstract

In recent years, first-principles modeling techniques have made tremendous advances. This allows researchers to estimate the various properties of materials and provide invaluable insights into the physical processes from a microscopic perspective, which cannot directly be assessable by experiments. With the continuing increasing computation powers, first-principles methods are expected to play a more important role in materials design. This chapter aims to serve as a battery-related computation handbook for general readers who may be new to first-principles calculations. Specifically, this chapter will introduce the well-established ab initio modeling methods widely used in battery-related studies from both the thermodynamic and kinetics aspects. The thermodynamic

I.-H. Chu · M. Zhang · S. P. Ong (✉) · Y. S. Meng (✉)
Department of NanoEngineering, University of California San Diego, La Jolla, CA, USA
e-mail: ihchu@eng.ucsd.edu; johnson1228@gmail.com; miz016@eng.ucsd.edu; ongsp@eng.ucsd.edu; shirleymeng@ucsd.edu

W. Andreoni, S. Yip (eds.), *Handbook of Materials Modeling*,
https://doi.org/10.1007/978-3-319-50257-1_96-1

approaches that will be discussed include the computations of equilibrium voltage and voltage profiles, electronic structure, and stability analyses. The kinetics approaches will cover common methods for ionic diffusion studies: transition state theory and nudged elastic band method and ab initio molecular dynamics. This is followed by the conclusion and outlook.

Keywords
Alkali-ion battery · Electrodes · Electrolytes · Interfaces · First-principles modeling · Voltage profile · Electronic structure · Phase stability · Surface · Defects · Ab initio molecular dynamics · Ion diffusion · Nudged elastic band · Transition state theory

1 Introduction

Global warming coupled with energy demand has made the development of renewable energy technologies (solar, geothermal, tidal, wind, etc.) a global interest and major concern. However, most renewable energy technologies suffer from high variability and mismatch between demand and supply. Reliable and cost-effective electrical energy storage is therefore a crucial enabler to renewables, as well as nonpolluting means of transportation (Lewis 2007). Among the multitude of energy storage technologies (e.g., zinc-manganese battery, nickel-cadmium battery, nickel-hydrogen battery, lead-acid battery, alkali-ion battery, fuel cell, redox flow battery, etc.), the rechargeable alkali-ion battery has emerged as one of the most attractive candidates for grid and vehicular applications and the dominant one for mobile consumer applications, due to its high specific energy, high operation voltage, wide working temperature, and long cycle life (Tarascon and Armand 2001).

A rechargeable battery comprises two electrodes – the cathode and the anode – separated by an electrolyte (Fig. 1). Alkali ions shuttle between the two electrodes, with the electrolyte acting as an alkali-ion conductor and electrical insulator. During discharge, alkali ions (A^+ in Fig. 1) are extracted from anode and inserted to the cathode, passing through the electrolyte in the process. Meanwhile, electrons pass through the external circuit to perform work. The reverse process occurs during charge.

The energy contained in any battery is the integral of the voltage multiplied by the charge capacity. To achieve high-energy and high-power density for long cycling life in alkali-ion battery, the electrode should have high specific capacity (charge stored per unit mass or volume), high operating voltage, reasonable electron and ionic conductivity, and good phase and electrochemical stability. Suitable electrolyte selection for a pair of electrodes in alkali-ion battery is another important aspect. To prevent the reduction and oxidation of the electrolyte, it is necessary that Fermi level of anode should be lower in energy than the lowest unoccupied molecular orbital (LUMO) of the electrolyte, while Fermi level of the cathode should be higher in energy than the highest occupied molecular orbital (HOMO) of the

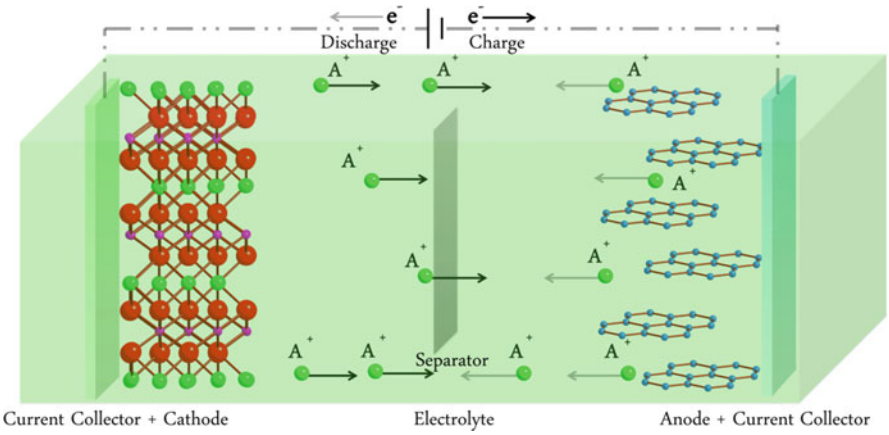

Fig. 1 Schematic of a rechargeable alkali-ion battery with transition metal oxide as cathode (green, alkali-ion; purple, TM; red, oxygen ion), carbon-based material as anode

electrolyte (Roy and Srivastava 2015). In the context of solid-state electrolytes, LUMO (HOMO) is referred to as the conduction band minimum (valence band maximum). Additionally, the electrolyte, especially for the solid-state electrolyte, is expected to have good interfacial stability, facile ion conductions which are more stringent than electrodes, and excellent electronic insulations.

Due to the significant advances in computation power in recent years, computer simulations have become an important complementary tool kit to experiments for the understanding and design of materials. First-principles density functional theory (DFT), (Hohenberg and Kohn 1964) especially the framework developed by Kohn and Sham (1965) that evaluates various properties of materials by solving single-particle Kohn-Sham equation with minimal approximation, has been particularly successful in this context. First-principles calculations allow researchers to evaluate the key properties of materials from an atomistic level, and hence provide invaluable insights into the fundamental physical processes that may not be directly assessable by experiments. Moreover, computation-guided discovery of novel materials has made tremendous progress for energy applications, including new alkali-ion battery materials (Deng et al. 2016; Urban et al. 2016). This is facilitated not only by the increasing computer power but also the development of the automated high-throughput first-principles screening that allows rapid identification of the most promising candidates from a pool of hundreds of thousands of initial candidates.

In the following sections, we will give a general introduction of well-established first-principles modeling techniques used to elucidate the thermodynamics and kinetics of battery materials.

2 Thermodynamic Approaches

2.1 Equilibrium Voltage

The operating voltage is a key metric of a battery to evaluate the stored energy density. By definition, the voltage difference between electrodes of a battery is equal to the difference in electron electrochemical potentials of the electrodes:

$$V = -\frac{\eta_{e^-}^{cathode} - \eta_{e^-}^{anode}}{e} \tag{1}$$

where $\eta_{e^-}^{cathode}$ and $\eta_{e^-}^{anode}$ are the electrochemical potentials of electrons (Fermi levels) in the cathode and anode. Inserting alkali chemical potential in any material, $\mu_A^X = \eta_{e^-}^X + \eta_{A^+}^X$, into Eq. 1 yields:

$$V = -\frac{\left(\mu_A^{cathode} - \mu_A^{anode}\right) - \left(\eta_{A^+}^{cathode} - \eta_{A^+}^{anode}\right)}{e} \tag{2}$$

where $\eta_{A^+}^{cathode}$ and $\eta_{A^+}^{anode}$ are the electrochemical potentials of alkali-ion in the cathode and anode. When a battery is at thermodynamic equilibrium ($\eta_{A^+}^{cathode} = \eta_{A^+}^{anode}$), the voltage difference between electrodes can be expressed in terms of the difference in alkali chemical potential:

$$V = -\frac{\mu_A^{cathode} - \mu_A^{anode}}{\mathrm{z}F} \tag{3}$$

where z is the amount of charge transferred, and F is the Faraday constant. By definition, $\mu_A = dG/dN_A$ is the change of the Gibbs free energy of the electrode material with alkali-ion concentration (Aydinol et al. 1997). The voltage is thus a function of free energy change of the overall cathode/anode reactions (Nernst equation):

$$\overline{V} = -\frac{\Delta G_r}{\mathrm{z}F} \tag{4}$$

where $\overline{V}$ is the average voltage by considering over a finite amount of reactions between cathode and anode.

Assuming that the entropic and volumetric effects are small at low temperature, the Gibbs free energy change for alkali insertion is often approximated by the DFT total energy difference for two alkali-ion concentrations $\Delta G_r = \Delta E_r + p\Delta V_r - \mathrm{T}\Delta S_r \approx \Delta E_r$. Taking the lithium-layered oxide cathode $\mathrm{Li}_x\mathrm{MO}_2$ with a Li metal anode as an example, the overall reaction is given as follows:

$$\mathrm{Li}_{x2}\mathrm{MO}_2 + (x_1 - x_2)\,\mathrm{Li} \rightarrow \mathrm{Li}_{x1}\mathrm{MO}_2 \tag{5}$$

with $x_1 > x_2$. Then the reaction voltage can be calculated as:

$$V_{(x_1,x_2)} \approx -\frac{E\left(\mathrm{Li}_{x_1}\mathrm{MO}_2\right) - E\left(\mathrm{Li}_{x_2}\mathrm{MO}_2\right) - (x_1 - x_2)\,E\,(\mathrm{Li})}{(x_1 - x_2)\,F} \tag{6}$$

The energies of $\mathrm{Li}_x\mathrm{MO}_2$, MO_2, and Li can be obtained via DFT total energy calculations. This approximation is not limited to insertion or intercalation electrodes but can also be applied to conversion or alloy reactions.

Most early DFT calculations of average voltage for battery materials were based either on the local density approximation (LDA) or the generalized gradient approximation (GGA) for the exchange-correlation potential (Kohn and Sham 1965; Langreth and Mehl 1983). However, for the modeling of reactions involving changes in electronic states, neither LDA nor GGA are good approximations due to improper cancelation of self-interaction error. Many TM oxides have strongly localized *d* electrons at the metal center, which leads to the large error of voltage predicting based on LDA or GGA functional. In this regard, an inclusion of a Hubbard *U* in DFT calculations (aka DFT + *U*) was developed in the 1990s that significantly improves the DFT results for the system with strong correlated electronic structure (Anisimov et al. 1991, 1993). The method is controlled by Hubbard *U* parameter, which can be derived for each species either self-consistently (Cococcioni and de Gironcoli 2005) or more often, via fitting to experimental properties such as the oxide formation energy. The idea is borrowed from the Hubbard model in solid-state physics, to describe the transition between conducting and insulating systems. The larger the *U* value, the greater the penalty for shared electrons, driving the system toward integer electronic occupations (Cococcioni and de Gironcoli 2005). With proper choice of the *U* parameter, DFT + *U* calculations significantly improve the accuracy of predicted voltages over pure LDA or GGA for TM oxides (Zhou et al. 2004). More recently, DFT calculations using screened hybrid functionals, such as the Heyd-Scuseria-Ernzerhof (HSE) functional, (Heyd and Scuseria 2004; Heyd et al. 2003, 2006) have been shown to yield a similar accuracy as GGA + *U* without the need for an adjustable *U* parameter, though at significantly higher computational cost. A detailed comparison of calculated voltages for lithium TM oxides with GGA, GGA + *U*, and HSE06 can be found in an earlier work by Chevrier et al. (2010)

2.2 Voltage Profile

Calculating the voltage profile requires the knowledge of stable intermediate phases during alkalination/de-alkalination process. The formation energy calculations allow one to determine the ground state energy of the stable phase at all intermediate concentrations. Taking the layered transition metal oxide $\mathrm{Li}_x\mathrm{CoO}_2$ as an example, the formation energy with respect to the stable end members (LiCoO_2 and CoO_2) is expressed as:

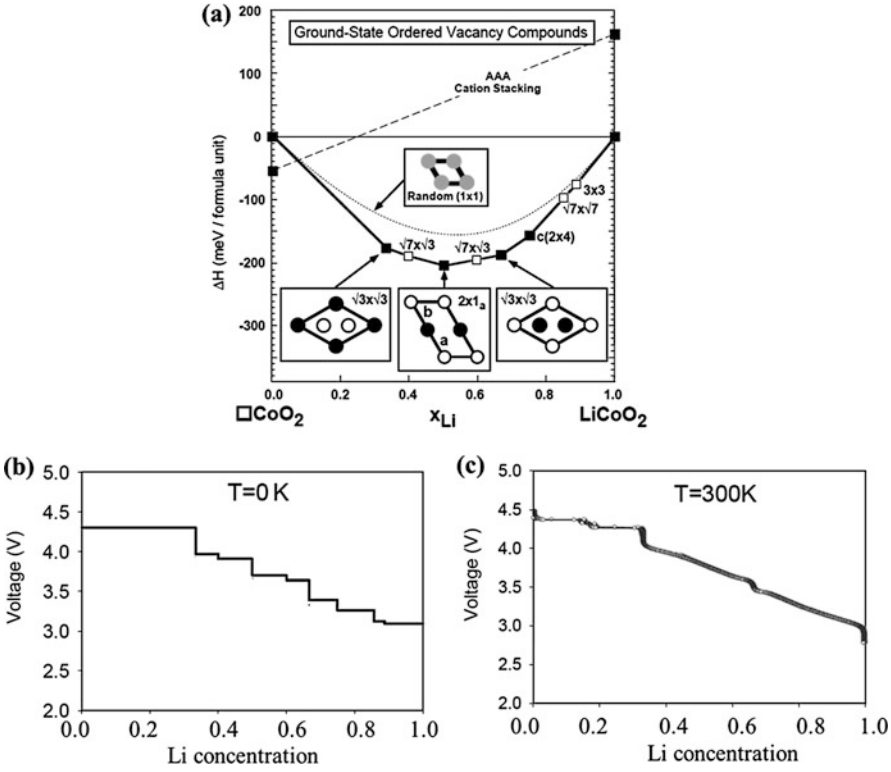

Fig. 2 (**a**) Stability convex hull (black line) of Li_xCoO_2. Filled square, DFT results; open square, cluster expansion results; filled circles, Li atoms; empty circles, Li-vacancy. (**b**) Predicted Li intercalation voltage of the Li_xCoO_2/Li cell as a function of Li concentration at T = 0 K. (**c**) Equilibrium voltage profile at T = 300 K calculated from Monte Carlo simulations. (Reproduced from Ref. (Wolverton and Zunger 1998) with permission. Copyright (1998) American Physical Society)

$$E_f\left(\mathrm{Li}_x\mathrm{CoO}_2\right) = E\left(\mathrm{Li}_x\mathrm{CoO}_2\right) - xE\left(\mathrm{LiCoO}_2\right) - (1-x)\,E\left(\mathrm{CoO}_2\right) \tag{7}$$

The resulting DFT-computed formation energy vs. composition curve (convex hull) is generated as shown in Fig. 2a. In this pseudo-binary stability diagram, the intermediate phases that are thermodynamically stable with respect to the end members ($LiCoO_2$ and CoO_2) form the convex hull. When the energy of an intermediate phase is above the convex hull (e.g., the dotted line in the figure), it implies that such intermediate phase is energetically unstable against its adjacent stable intermediate phases (filled and open squares in the figure) on the convex hull. At each concentration, different configurations of Li-vacancies and oxygen stacking sequence are considered. Examples of some of the predicted Li-vacancy ordering in Li_xCoO_2 are also illustrated in the figure. After the stable intermediate phases are

identified, stepwise average voltage can be computed based on Eq. 6, which leads to the voltage profile in Fig. 2b.

It should be noted that the DFT-computed voltage is an approximation without considering entropic effects, and the accessible alkali orderings are also limited by the supercell size utilized. These approximations work reasonably well for average voltages, especially for two-phase reactions involving ordered phases (e.g., olivine $LiFePO_4$). To obtain a full voltage profile and account for the configurational entropy (important for solid solution regions), one approach is to fit the DFT energies of a large number of alkali concentrations and orderings for a host material to a cluster expansion Hamiltonian. As shown in Fig. 2a, additional stable intermediate phases of Li_xCoO_2 (indicated by open squares on the black line) are discovered by using such approach. The key assumption here is that the contribution to free energy from the other degrees of freedom (e.g., vibrational, electronic) is insignificant and can be coarse-grained out. Monte Carlo simulations, e.g., using the Metropolis algorithm, can then be carried out using the Hamiltonian to sample the configurational space and evaluate finite temperature voltage profile. Details of the cluster expansion method and Monte Carlo simulation can be found in some excellent reviews (Urban et al. 2016; Meng and Arroyo-de Dompablo 2009). As an example, Wolverton and Zunger applied first-principles-based cluster expansion and Monte Carlo methods to model the Li-vacancy orderings in Li_xCoO_2, resulting in the temperature-dependent voltage profiles (see Fig. 2b and c for $T = 0$ and 300 K). Temperature effect mainly results in a continuous voltage slope, which smooths out the voltage steps that are present in the 0 K limit.

2.3 Electronic Structure

The relative energies of electronic levels for different components in alkali-ion battery determine the limitation of the stored energy. Figure 3a schematizes the relation between the equilibrium voltage and electronic structures of the electrode, electrolyte. At open circuit condition, the energy difference of Fermi levels between the anode and cathode builds electron electrochemical potentials. Assuming there is no electrode/electrolyte reaction, this electron potential difference equals the difference in alkali chemical potential between the anode and cathode, which is measured as open circuit voltage (V_{OC}). Once charging current is applied, electrons are further pumped out from the valence band of cathode through the circuit to the conduction band of the anode, resulting in the downshift and upshift for the Fermi level of cathode and anode, respectively. Alkali ions are extracted from cathode to the anode with the oxidation change of other ions, e.g., TM ions to balance the charge. The whole process is fully reversible during the discharging process in an ideal case. The redox potential (V_{redox}) measured during charging/discharging process is limited by the "window" of the electrolyte. If the potential of the anode and cathode shift beyond the LUMO and HOMO of the electrolyte, the electrolyte is reduced on the anode and oxidized on the cathode to form the solid electrolyte interphase (SEI). The ideal SEI is an ionic conductor and an electron insulator,

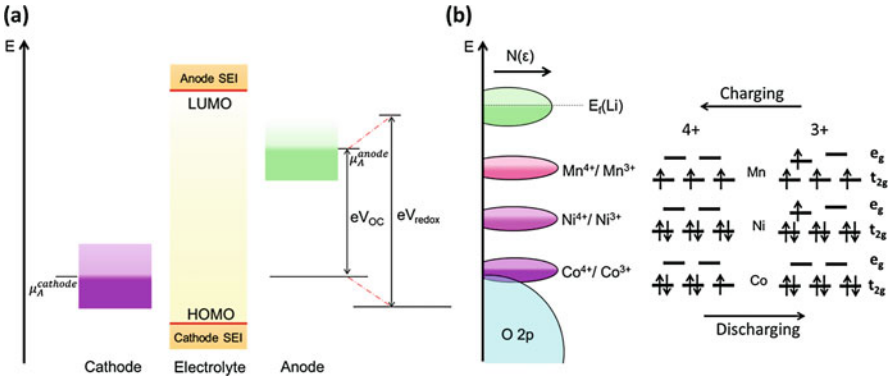

Fig. 3 (**a**) Relative energies of the electrolyte window and the electrode chemical potentials $\mu_A^{cathode}$ and μ_A^{anode} with no electrode/electrolyte reaction. (b) Relative positions of energy levels and typical electron configurations in layered Ni-Mn-Co oxide cathode

which prevents further decomposition of the electrolyte and thus increases stable voltage window.

The electronic levels of the electrode involved in the redox reaction arise from the *d*-states of the TM cations in most cases. The Fermi level energy as well as the density of states (DOS) near the Fermi level for redox center can be obtained from DFT calculations. Figure 3b qualitatively summarizes the positions of the redox active energy levels for Co^{4+}/Co^{3+}, Ni^{4+}/Ni^{3+}, and Mn^{4+}/Mn^{3+}, as well as the oxygen 2*p* band in TM oxides. In most of the structures including layered, spinel, and disordered rock salt, TM ions occupy octahedral sites that are coordinated by six oxygen atoms. Based on crystal field theory, TM five *d* orbitals split into two sets of levels labeled t_{2g} and e_g as shown in Fig. 3b. Each of the level can hold two electrons with opposite spin. The commonly observed electronic configurations of *d* orbitals for Co^{4+}/Co^{3+}, Ni^{4+}/Ni^{3+}, and Mn^{4+}/Mn^{3+} are also illustrated in Fig. 3b. The lone electron in e_g level triggers Jahn-Teller distortion, breaking the degeneracy between the two e_g orbitals to lower the overall energy for the case of Mn^{3+} and Ni^{3+}. When the battery is charged, TM cations are oxidized to 4+ from 3+, and they are reduced back to +3 oxidation state as they receive electrons from the anode during discharging. More importantly, the Co^{3+}/Co^{4+} level is the lowest in energy because Co redox involves the more stable t_{2g} orbitals, while Ni and Mn redox involves the less stable e_g orbitals. This relative alignment of energy levels directly indicates redox reaction sequence of the electrode containing different TM ions since lower energy levels correspond to higher redox voltages.

Although the electronic structure is in general complex, it provides another key insight into the available number of electrons near Fermi level. If an alkali-ion is extracted from the cathode host structure, an electron is pumped out from the valence band at the same time. Therefore, the more the available number of electrons are, the higher the alkali-ion storage capacity is. In classical layered cathode, e.g., $LiCoO_2$ and $LiNi_{0.5}Mn_{0.5}O_2$, oxygen ions are coordinated by three Li and three

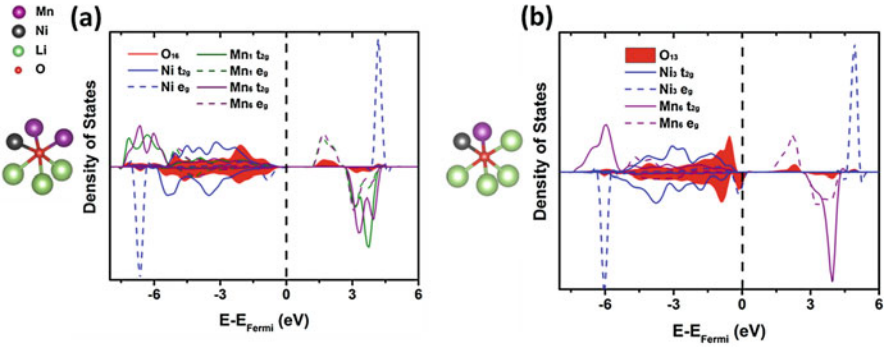

Fig. 4 An example of an oxygen site in the fully lithiated structure (**a**) without a Li-O-Li linear bond and (**b**) with a Li-O-Li linear bond, required for labile oxygen states

TM ions as shown in Fig. 4a. In this configuration, a much larger projected DOS originating from the TM states than from the O states between 0 and −1.5 eV below Fermi level (commercial organic liquid electrolyte window) is found, indicating that the redox reactions are dominated and restricted by the TM 3*d* electrons. On the other hand, Li-excess is created by the substitution of some TM by Li, leading to Li-O-Li configurations in many of the new exciting cathode materials. It shows an increased oxygen projected DOS below the Fermi level for oxygen with a linear Li-O-Li bond based on GGA + *U* calculations (see Fig. 4b). This labile oxygen observed computationally with increased projected DOS below the Fermi level paves the completely new research on anionic redox and breaks the bottleneck for reaching higher energy density in alkali-ion battery (Grimaud et al. 2016; Okubo and Yamada 2017).

The electronic band gap deduced from the calculated DOS is also useful to investigate the electronic properties of a potential electrode or solid electrolyte material. While high electronic conductivity for the electrode material is a necessary condition for high rate performance of alkali-ion battery, low electronic conductivity is required for the potential electrolyte materials. Similar to the voltage calculation, the introduction of a *U* correction term in the GGA method could substantially improve the accuracy of calculated band gaps (Zhou et al. 2004). Other helpful information that can be extracted from electronic structure analysis includes chemical bonding, orbital hybridization, magnetic properties, etc.

2.4 Stability Analyses

2.4.1 0 K Phase Stability

The pseudo-binary stability diagram mentioned in the previous subsection essentially works for electrode materials. In a general situation, the thermodynamic stability of any given compound (e.g., solid electrolyte) can be analyzed by

evaluating its decomposition energy referenced to the linear combinations of stable compounds in this compositional space. This can be achieved by constructing the convex hull using the DFT energy of all known compounds in this compositional space. In the case of olivine $LiFePO_4$, for example, the related stability analysis requires the DFT energies of all existing $Li_xFe_yP_zO_u$ compounds (x, y, z, and u are nonnegative integers) including itself in Li-Fe-P-O quaternary compositional space. The stability metric under this circumstance is called the energy above the hull (E_{hull}), (Sun et al. 2016; Ong et al. 2008) which measures how stable a compound is by measuring how high its energy is above the convex hull. It is always nonnegative, and it equals zero for stable compounds. The higher the E_{hull}, the more unstable the compound tends to be. With the advent of large open-source materials databases such as the Materials Project (Jain et al. 2013), a common approach is to leverage on pre-computed DFT energies in these databases for compounds other than that of primary interest, which significantly reduce the computational effort involved, especially for high-dimension compositional space. E_{hull} is frequently adopted as an efficient descriptor for phase stability and synthesizability in high-throughput first-principles screening studies to rapidly rule out structures that are unlikely stable at ambient temperatures (high E_{hull}).

2.4.2 Surface Stability

The real surface configuration rarely coincides with the ideal lattice plane which is a geometrical abstraction of the crystal structure. In reality, the stable surface can contain charged species adsorbed from the environment, charge density rearrangement, and stepped or kinked surface profile. This makes determination of surface thermodynamics very challenging. For this reason, first-principles calculations can be a useful tool to determine facet-specific surface energies. The standard model to calculate surface energies is a two-dimensional surface slab with bulk stoichiometry oriented to expose the facet of interest, with a sufficiently large vacuum layer added on top of the slab to ensure that there is minimal interaction between the slab and its periodic images along the surface normal. The k-point grid for surface slab is thus generated as $k_1 \times k_2 \times 1$, which assures no energy dispersion in the direction out of the surface.

Standard procedures of generating surface slabs include basis transformation, atomic coordinates rescaling, termination choice, and polarity check. Surfaces are typically defined using the Miller index notation by the conventional unit cell. However, first-principles calculation requires the basal plane to be coincident with the constructed slab surface. The basis of the conventional unit cell has to be transformed so that (001) plane of the new basis is parallel to the Miller plane of interest. The third vector should be as orthogonal to the basal plane as possible with a relatively short length. The atomic coordinates are then redefined based on the new basis. For a given surface orientation, a number of termination layers usually exist due to different atomic configurations and can be chosen by placing the basis at different positions along the third vector. Note that a charged surface with a perpendicular dipole moment in a repeated unit (type III according to surfaces classification by Tasker) produces a polarizing electric field in the bulk, leading to

infinite periodic cell energies (Tasker 1979). For example, the (111) face of NiO ionic crystal has alternating layers of Ni^{2+} and O^{2-} ions, which forms a permanent dipole moment perpendicular to the surface. Atomic reconstruction by moving half the charged species on one surface to the other side to cancel out the 2D-dipole is a common approach (the so-called Tasker III to Tasker II reconstruction) to stabilize type III surface (Bruno 2013).

From DFT calculations, the surface energy can be computed using the following expression:

$$\gamma = \frac{1}{2A}\left[E\left(slab\right) - N \cdot E\left(bulk\right)\right] \tag{8}$$

where A is the surface area of the slab, E(slab) is the surface slab energy, E(bulk) is the bulk energy per atom, and N is the number of atoms in the surface slab. The prefactor 1/2 comes from the fact that each surface slab contains two equivalent surfaces. The Wulff shape, which is the equilibrium shape of the crystal, can be constructed using the lowest surface energies of different facets. The larger the surface area of a facet contributes to the Wulff shape, the more stable that facet tends to be. As an example, surface properties of olivine $LiFePO_4$ cathode were studied by Wang and co-workers (Wang et al. 2007). The two low-energy surfaces (010) and (201) are found to make up almost 85% of the surface area of Wulff crystal shape. More importantly, redox potential for the (010) surface was calculated to be much lower than the bulk value, which shows the anisotropic property of surface redox potentials. This study pinpoints the effect of surface energies and crystal shape on the electrochemistry for electrode materials composed of particles at nanoscale. Surface electronic structure, surface reconstruction, and adsorbate interactions can also be studied based on surface stability calculations.

2.4.3 Electrolyte/Electrode Interface Stability

Understanding of electrolyte/electrode interfaces has become a recent focus of the greatest importance for the performance improvement of electrochemical energy storage systems. For alkali-ion batteries with liquid organic electrolyte, SEI formation due to electrolyte decomposition is critical to cycling performance and safety. For all solid-state alkali-ion batteries with sulfide-type electrolytes, the rate-determining process is usually observed around the cathode/electrolyte interfaces. To predict the electrode/electrolyte interface stability under large variations in environmental conditions is one of the grand challenges for battery study. First-principles calculation using DFT-based methods has been developed to investigate most stable interfacial matching of two crystal solids (Haruyama et al. 2014). In a traditional manner, the procedure to investigate the interface formed by two compounds comprises three major steps: (i) identify the lowest-energy surface facet of each material as detailed in surface stability calculations; (ii) patch the two surface slabs using a reasonably large supercell (with a vacuum layer of 10 Å) to ensure as small lattice parameter misfit as possible; and (iii) enumerate all possible configurations for the interface supercell including slide of one surface slab with

respect to the other, and perform DFT relaxations. The alkali-ion sites and alkali-ion transfer properties in the most stable interface can then be further investigated under different thermodynamic equilibrium conditions.

The explicit interface calculations often require very high computational cost because of the supercell used. For studies of electrolyte/electrode interfacial stability, a critical step is to identify the possible reaction products formed at the interface. In the case of solid electrolyte/electrode interfaces, there are two efficient analysis methods based on two different thermodynamic approximations for such purposes (Zhu et al. 2015a; Richards et al. 2016; Tang et al. 2018).

- *Fast ionic diffusion limit*: In this approximation, the diffusing ions in the solid electrolyte are assumed to be the main mobile species. Under such conditions, the interface can be modeled as an open system with respect to the mobile species. The relevant thermodynamic potential is the grand potential. Taking the Li-ion solid electrolyte as a concrete example, the Li grand potential is expressed as $\varphi = E - \mu_{Li}N_{Li}$, where E, N_{Li}, and μ_{Li} are, respectively, the internal energy, the number of Li atoms in the open system, and the Li chemical potential. When the metallic Li is taken as the anode, the Li solid electrolyte/anode interface is modeled as the solid electrolyte at high $\mu_{Li} \approx \mu_{Li0}$, and the Li solid electrolyte/cathode interface is modeled as the solid electrolyte at low $\mu_{Li} \approx \mu_{Li0} - V$, where V is the cell voltage and μ_{Li0} as the chemical potential in metallic Li.
- *Multi-species equilibrium*: The second method assumes full thermodynamic equilibrium between the solid electrolyte and electrode in varying electrolyte/electrode compositional ratios x (between 0 and 1). Specifically, the equilibrium composition at a given ratio x corresponds to $c_{\text{electrolyte}}x + c_{\text{electrode}}(1 - x)$ with c_y being the composition of compound y. To estimate the likely reaction products at different x values, a pseudo-binary stability diagram that is like the aforementioned stability diagram for electrode materials is constructed. In this pseudo-binary stability diagram, however, the x values correspond to the compositional ratio x, whereas y values are the associated reaction energy which reaction products have the same composition as $c_{\text{electrolyte}}x + c_{\text{electrode}}(1 - x)$. This approach tends to be more reflective of the conditions during actual synthesis and assembly conditions.

Note that the approaches presented here are within thermodynamic approximations. To capture the kinetic effects on the formation of electrolyte/electrode interfaces, computationally more demanding approaches, e.g., ab initio molecular dynamics can be adopted (see Sect. 3.2.6).

2.4.4 Defects and Dopability

Extrinsic doping is a common strategy to further optimize battery material properties, such as phase stability, ionic and electronic conductivity, and cost. It is crucial to predict the feasibility of introducing a dopant into a crystal structure based on first-principles calculation. The size of the supercell model is inversely

proportional to the dopant concentration. Note that different types of doping, including substitutional, interstitial, and anti-site, need to be considered for the supercell construction. Generally speaking, the dopability of a species depends on its ionic radius and oxidation state relative to existing species in the crystal. In the case of charge balance doping, the neutral dopant formation energy can be defined as follows:

$$E_f\,(\text{doped}) = E\,(\text{doped}) - E\,(\text{pristine}) - \sum_{i=1}^{N} n_i \mu_i \tag{9}$$

where E(doped) and E(pristine) are the energies of the structure with and without the neutral dopant, respectively, μ_{i} is the atomic chemical potential of species i, n_i is the number of atoms of species i being added or removed, and N is the total number of species in the doped structure. Synthesis condition can be selected based on the energy calculation to tune species chemical potential so that the formation energy can be low enough to prevent any species precipitation. Additionally, the doped structure should remain stable without any decomposition during synthesis.

3 Kinetics Approaches

There are two widely used first-principles approaches that can assess the kinetics of alkali-ion diffusion in battery materials: transition state theory-based methods such as the nudged elastic band approach and ab initio molecular dynamics simulations. In the following, we will present the key concept of each approach for ionic diffusion studies as well as their limitations.

3.1 Transition State Theory and the Nudged Elastic Band Method

In materials where the equilibrium lattice sites are well defined, the ionic diffusion can be investigated using transition state theory. From an atomistic viewpoint, diffusion can be viewed as a series of hopping events of ions between neighboring sites. In each hop, an ion migrates from one site to its neighboring vacant site via an activated state (aka the transition state), which has the highest Gibbs free energy along the minimum energy path between the two sites. Based on the transition state theory (Deng et al. 2016; Urban et al. 2016), the rate k at which the hopping event occurs can be expressed as:

$$k(T) = \upsilon^*(T) e^{-\frac{\Delta G_a(T)}{k_B T}} \tag{10}$$

$$\Delta G_a(T) = G_a(T) - G_i(T) \tag{11}$$

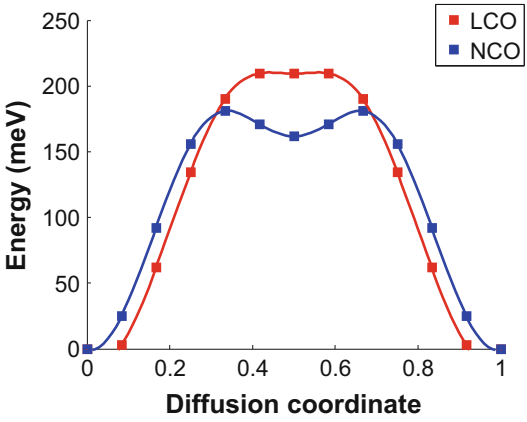

Fig. 5 An example of NEB computed migration barriers. The two example structures are $LiCoO_2$ (LCO) and $NaCoO_2$ (NCO). (Reproduced from Ref. (Ong et al. 2011) with permission. Copyright (2011) Royal Society of Chemistry)

Here, $\Delta G_a(T)$ is known as the activation barrier, and it is the difference of the Gibbs free energies at the activated state ($G_a(T)$) and initial state ($G_i(T)$). $\upsilon^*(T)$ is the effective attempt frequency at temperature T. In the dilute limit of carrier concentration, the diffusivity can be approximated as $D(T)\ d^2k(T)$ where d is the hopping distance (assumed to be known). Moreover, the attempt frequency $\upsilon^*(T)$ is often assumed to be temperature-independent, and the typical values fall between 10^{11} and $10^{13}\ s^{-1}$ (Urban et al. 2016). When the diffusivity follows the Arrhenius relation (see Eq. 18 below), the activation barrier in Eqs. 10 and 11, $\Delta G_a(T)$, can be assumed to be temperature independent. When the entropic effects become negligible, $\Delta G_a(T)$ can be further approximated as DFT energy difference between the activated state and the initial state ($\Delta G_a(T) \approx \Delta E_a$).

For ionic diffusion studies, the nudged elastic band (NEB) method (Jonsson et al. 1998) is a widely used approach to determine the 0 K activation barriers of the ion migration paths for a given atomic configuration. This approach requires the initial and final states of the migration path (aka end points) as input, from which a given set of intermediate states (aka images) are generated to serve as the initial guess of the migration path. The minimum energy path is determined by minimizing the atomic forces in all the images subject to the constraint of a harmonic coupling (in terms of harmonic springs) between adjacent images. In the end, the activation barrier (ΔE_a) is computed as $\Delta E_a = E_{\max} - E_i$ where $E_{\max}$ is the highest energy along the optimized migration path and E_i is the energy of the initial state. An example of NEB results is shown in Fig. 5 for layered oxides $ACoO_2$ (A = Li and Na) (Ong et al. 2011).

In a typical NEB calculation, it essentially comprises the following four steps:

1. Initial structural optimization calculations of the pristine crystal structure.
2. Structural optimizations of the two initial and final state structures.

3. An interpolation between the initial and final states to generate a set of images along the migration path. The linear interpolation is the most commonly used scheme for such purpose.
4. An NEB calculation to find the lowest-energy migration path, from which the highest energy is determined, and hence the activation barrier.

In the studies of ionic diffusion, the NEB method can be applied to evaluate the barrier of any given migration path. This makes it particularly useful to probe the effects of local environment (e.g., local arrangement of the framework) on the ionic diffusion. Indeed, the NEB calculations have been employed to understand the diffusion mechanisms in several important battery materials, e.g., layered $LiCoO_2$ and olivine $LiFePO_4$ cathodes (Deng et al. 2016; Urban et al. 2016). Moreover, the migration barriers from NEB calculations can also serve as inputs for other techniques, including the kinetic Monte Carlo (KMC) simulations. This is a Monte Carlo simulation method that studies the time evolution of natural processes using lattice models, e.g., the diffusion of alkali ions in the battery materials. Using the local environment-dependent barriers from NEB calculations, a first-principles cluster expansion can be carried out to parameterize these barriers for Monte Carlo simulations. More details about the KMC method, including the basic steps in the simulations, can be found in literature (Deng et al. 2016; Urban et al. 2016).

3.1.1 Limitations of the NEB Method

In studies of alkali-ion batteries, the NEB method has been mainly applied to the bulk systems (pristine electrodes and solid electrolytes). In the case of noncrystalline systems, e.g., electrolyte/electrode interfaces, much higher computational efforts are inevitably required due to the large number of distinct ionic migration paths that need to be considered due to the lower symmetry. There are two further limitations of the NEB method compared to the ab initio molecular dynamics simulations (see Sect. 3.2).

First, the start and end points of the migration path must be specified as inputs for NEB calculations. For alkali battery materials with complex diffusion properties, e.g., when ionic motions are highly concerted (common in superionic conductor electrolytes), the identification of the relevant migration events and local environment become very challenging. In this scenario, ab initio molecular dynamics (see Sect. 3.2) becomes the more appropriate technique to use. For this reason, NEB calculations are primarily performed in dilute carrier limits, e.g., single alkali-ion vacancy migration in an otherwise fully alkaliated structure or single alkali migration in an otherwise alkali-ion-free framework structure.

Second, NEB calculations essentially output the migration barrier at 0 K, i.e., the temperature effects are not considered in the calculations. Besides, to estimate an accurate hopping rate associated with the migration path, and hence the diffusivity, the prefactor in Eq. 10 must be computed explicitly. However, it is often assumed to be some value between 10^{11} and $10^{13}\ s^{-1}$.

3.2 Ab Initio Molecular Dynamics Simulations

Molecular dynamics (MD) simulates the atomic motions at finite temperatures by integrating the Newtonian equations of motions. A key input of this approach is the description of the interatomic interactions, whereas the main output is the trajectories of the atomic motions. Depending on how the interatomic interactions are obtained, MD simulations can be categorized into two general classes: classical MD and ab initio MD (AIMD) simulations. In classical MD simulations, the interatomic interactions are expressed in terms of analytical functions with parameters fitted using either experimental or first-principles data, whereas in AIMD simulations, the interatomic interactions are obtained by directly solving the Schrödinger equation with approximations.

Although classical MD simulations are computationally less expensive than the ab initio counterpart, it does suffer from serious drawbacks stemming from the use of empirical potentials, e.g., poor transferability across different chemistries, and the difficulty in dealing with complex interatomic interactions with simple function forms. On the other hand, AIMD simulations can generally be applied across broad chemical spaces, and the accuracy of the interatomic interactions is essentially limited by the underlying approximations of the ab initio approach.

There are two main variants of AIMD models today: Born-Oppenheimer (BO) variant and Car-Parrinello (CP) variant (Car and Parrinello 1985; Hutter 2012). For battery-related studies, the former variant is more commonly adopted. The theory behind these AIMD techniques is beyond the scope of this chapter and is extensively covered by many excellent textbooks and reviews (Hutter 2012; Marx and Parrinello 1996). The main disadvantage of AIMD methods is the significantly higher computational cost compared to the classical MD, and also the NEB method (Sect. 3.1). This places constraints on the accessible cell size as well as time scale in AIMD simulations. However, these can be mitigated by the advances in computer power and the nature of the problem under investigation.

The key output from AIMD simulations is the trajectories of ionic motions, from which the diffusion properties of materials, e.g., ionic diffusivity and conductivity, can be evaluated. The AIMD technique has gained tremendous successes in the studies of alkali-ion battery materials, particularly for the understanding and discovering novel alkali-ion superionic conductors. In the following, we will first sketch the well-established analysis methods and how they are applied to understand the ionic diffusions in battery materials. We will also discuss practical considerations on the parameter selection, the applications of AIMD in electrolyte/electrode interfaces, and the limitation of this technique. We should stress that these analysis approaches are agnostic of the types of MD simulations (i.e., classical and ab initio), and they are also applicable to other classes of materials, e.g., oxygen conductors in solid oxide fuel cells.

3.2.1 Ionic Diffusion and Conduction Coefficients

For a given 3D crystal structure with N mobile ions, the self-diffusion coefficient can be computed from AIMD simulations by evaluating the velocity-velocity autocorrelation function (Green-Kubo relation):

$$D^* = \frac{1}{3N}\int_0^\infty dt \sum_{i=1}^{N} \left\langle \vec{v_i}\,(t_0) \cdot \vec{v_i}\,(t+t_0) \right\rangle_{t0} \tag{12}$$

where $\vec{v}\,(t)$ is the velocity of ion i at time t and angular bracket in the integrand stands for an ensemble average over the initial time argument t_0.

This quantity is more frequently estimated from the ionic displacements via the Einstein equation:

$$D^* = \frac{1}{2dt}\lim_{t\to\infty} \frac{\partial \Delta \vec{r}\,(t)^2}{\partial t} \tag{13}$$

$$\Delta \vec{r}\,(t)^2 = \frac{1}{N}\left\langle \sum_{i=1}^{N} \left[\vec{r}_i\,(t+t_0) - \vec{r}_i\,(t_0) \right]^2 \right\rangle_{t0} \tag{14}$$

Here, $\vec{r_0}(t)$ is the position of mobile ion i, and $\Delta \vec{r}\,(t)^2$ is known as the mean square displacement (MSD) of the mobile ions over time t as an ensemble average over the initial time argument t_0.

We should stress that the two expressions (Eqs. 12 and 13) for the self-diffusion coefficient D^* are equivalent. However, due to the short accessible time scales in AIMD simulations that are limited up to a few hundred picoseconds in most cases, the convergence speed becomes an important factor to consider when computing the diffusion coefficient. In this context, Eq. 13 is more commonly adopted for computing D^* because it tends to converge more rapidly than that of Eq. 12 due to the averaging of the square displacements. Moreover, the long-time tail of the integral in Eq. 12 may also cause numerical inaccuracy when evaluating the diffusion coefficient in a short simulation time scale.

With the diffusion coefficient at temperature T in hand, the ionic conductivity can be estimated using the Nernst-Einstein equation expressed below,

$$\sigma(T) = \frac{\rho z^2 F^2}{RT} D^*(T) \tag{15}$$

Here, ρ and z are, respectively, the molar density and charge of the mobile ions in the simulation cell. For example, $z = +1$ for alkali ions such as Li^+ and Na^+. F and R are the Faraday constant and the gas constant, respectively. We should point out that since the computed D^* corresponds to the tracer diffusivity in experiments, the conductivity derived from Eq. 15 assumes no correlations in ionic motions. Here,

the correlation essentially describes how the displacement of one ion depends on those of other ions during the diffusion.

In many situations, such ionic correlation can be measured in terms of Haven ratio H_R, (Murch 1982)

$$H_R = \frac{D^*}{D_\sigma} \tag{16}$$

where D_σ is known as charge diffusivity defined below:

$$D_\sigma = \frac{1}{6N} \lim_{t\to\infty} \frac{\partial}{\partial t} \left\langle \left\{ \sum_{i=1}^{N} \left[\vec{r}_i\,(t+t_0) - \vec{r}_i\,(t_0) \right] \right\}^2 \right\rangle_{t0} \tag{17}$$

The Haven ratio equals one when the ionic motions are uncorrelated, while it is less than 1 for correlated ionic motions. For fast ionic conductors, H_R typically falls between 0.3 and 0.6 (Morgan and Madden 2014; Bron et al. 2013). Given the fact that the convergence of D_σ in any molecular dynamics simulations is usually much slower than that of D^*, there have only been few AIMD studies that attempt to explicitly estimate the H_R value.

3.2.2 Activation Energy

Apart from the ionic diffusivity and conductivity, another key quantity of interest is the activation energy E_a. Under the assumption that there are no phase transitions, one can perform AIMD simulations at multiple temperatures and fit the temperature-dependent diffusivity D to the Arrhenius relationship:

$$D = D_0 e^{-E_a/kT} \tag{18}$$

Here, D_0 stands for the diffusivity at temperature $T \to \infty$, and k denotes the Boltzmann constant. One can obtain E_a via a linear fitting of the log of D vs. 1/T (see Fig. 6a as an example). We should note that AIMD simulations are usually performed at elevated temperatures, e.g., above 600 K, to increase the number of diffusion events. The diffusivity at ambient temperatures can also be obtained from Eq. 18 via linear extrapolation. Nevertheless, we should stress that the scheme implies that the fundamental diffusion mechanisms remain unchanged between the entire temperature range of interest.

3.2.3 Analysis of the Diffusion Process

Besides the ionic diffusivity and conductivity, the ionic trajectory data also provide rich details about diffusion process of ions, including the energy landscape in the battery material and the related diffusion pathways for the mobile ions. The latter information can be obtained by calculating the probability density function $P\left(\vec{r}, T\right)$, which is a function of both the temperature and a spatial 3D grid (typically a uniform grid). Specifically, for an input trajectory data with a given

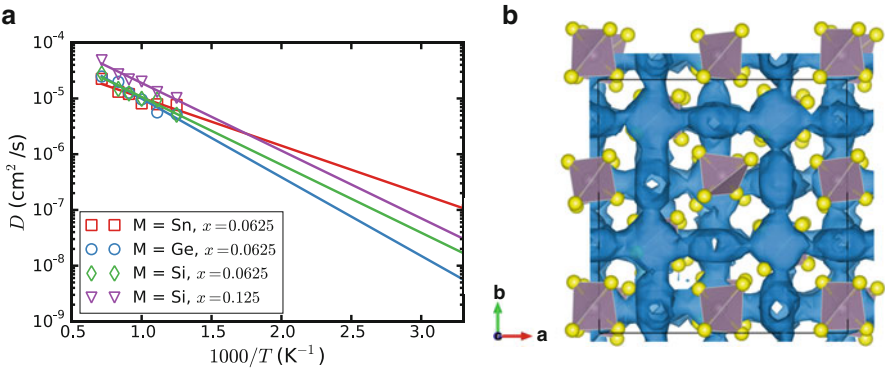

Fig. 6 (**a**) Arrhenius plot of doped structures $Na_{3+x}M_xP_{1-x}S_4$ (M = Si, Ge or Sn). (**b**) Isosurface (blue) of Na^+ probability density distribution P for $Na_{3.0625}Si_{0.0625}P_{0.9375}S_4$ at 800 K. (Reproduced from Ref. (Zhu et al. 2015b) with permission. Copyright (2015) American Chemical Society)

time scale and temperature T, P is computed by first counting the total number of mobile ions occupying each grid point using a distance-based algorithm. This is followed by a normalization such that $\int_0^{\Omega} P d\vec{r} = 1$ with Ω being the volume of the unit cell. Two useful pieces of information can be extracted from the probability density function: (1) low-energy sites (corresponding to higher $P\left(\vec{r}, T\right)$ values) at where the mobile ions prefer to reside and (2) pathways for the ionic diffusion. As an example, Fig. 6b demonstrates the Na^+ probability density function in cation-doped sodium superionic conductor Na_3PS_4. We should point out that the occupancies of the symmetrically distinct sites can also be estimated using this function, which provides useful message for further understanding the ionic diffusion process.

The Van Hove correlation function is a well-known technique to assess the ionic correlations during the diffusion process. Van Hove correlation function is often split into two parts, self-part G_S and distinct-part G_d, and they are expressed as follows:

$$G_s(r,t) = \frac{1}{4\pi r^2 N_d}\left\langle \sum_{i=1}^{N_d} \delta\left(r - |\vec{r}_i(t+t_0) - \vec{r}_i(t_0)|\right)\right\rangle_{t0} \tag{19}$$

$$G_d(r,t) = \frac{1}{4\pi r^2 \rho N_d}\left\langle \sum_{i\neq j}^{N_d} \delta\left(r - |\vec{r}_i(t_0) - \vec{r}_j(t+t_0)|\right)\right\rangle_{t0} \tag{20}$$

Here, $\delta(\cdot)$ refers to the 1D Dirac delta function. N_d and r are, respectively, the number of mobile ions in the unit cell and the radial distance. ρ is the number density for the mobile ions that is used as the normalization factor such that $G_d \to 1$ when $r \gg 1$. In terms of physical interpretation, the self-part $G_s(r,t)$ can be considered as

the probability density of a mobile ion that diffuses away from its initial position by a distance r after time t. The distinct-part $G_d(r, t)$ describes the radial distribution of $N_d - 1$ ions after time t with respect to the initial reference mobile ion. Note that when $t = 0$, $G_d(r, t)$ is reduced to the static pair distribution function.

3.2.4 Practical Considerations in AIMD Simulations

Since the AIMD techniques are computationally expensive, special care is required when selecting the relevant simulation parameters so that it achieves a good balance between the computational cost and the realistic results. In general, the selection of these parameters depends strongly on (i) the specific system under investigation, e.g., fast or slow conductors, and (ii) the type of problem of interest, e.g., comparative evaluation for systems with similar chemistries/topologies, or accurate diffusivity calculations. For any AIMD simulations of interest, key parameters include the simulation cell size, total simulation time, time step, simulation temperature, the ensemble, and so on. An inclusive summary about the parameter selection can be found in literature for interested readers (Shin and Saal 2018).

3.2.5 Modeling Electrolyte/Electrode Interfaces

AIMD simulations can also be used to explicitly model the electrolyte/electrode interfaces, which play a crucial role in the battery performance during charge-discharge process. To obtain more realistic results, the simulation supercell size for such systems is required to be much larger than the supercell for bulk materials, especially along the lattice direction normal to the interface. In principle, the diffusion properties at the interfaces may be estimated via AIMD simulations. However, that requires significant computational efforts due to the required large supercell and long simulation time scales. More often, AIMD simulations are applied to simulate the structural evolutions during alkaliation/de-alkaliation process (Leung and Budzien 2010) and the chemical reactions between the electrolyte (solid or liquid) and electrode materials from which the likely interfacial reaction products can be identified (Tang et al. 2018). In those simulations, a smaller supercell size with a shorter time scale may be utilized to speed up the AIMD simulations and obtain realistic results in a qualitative manner. Analysis tools have been developed in recent years that aim to efficiently determine the interfacial products from AIMD simulations. Among them include the radial distribution function (RDF) analysis. In that method, the RDFs of all possible products in their crystalline phases are compared to that of the interface to identify the likely reaction products. We should note that all these existing techniques are based on various approximations, and they are required for further improvements.

3.2.6 Limitation of AIMD Simulations

Similar to the NEB method, AIMD simulations are mainly applied to the *bulk* systems for their diffusion properties, especially the alkali-ion superionic conductors. For alkali-ion superionic conductors, key quantities such as ionic diffusivity and conductivity can often be estimated within the accessible AIMD time scale that is typically up to a few hundred picoseconds. For bulk electrode material such as alkali

transition-metal oxide cathodes, the presence of transition metals often requires spin polarization calculations. Also, the ionic conduction in the electrode materials is usually much slower than in the superionic conductors, implying that longer simulation time scale may be needed for properly converged ionic conductivity. Therefore, diffusion studies using AIMD simulations for these materials often require substantially higher computational cost, and key diffusion properties such as alkali-ion migration barriers and ionic conductivity are often estimated from NEB calculations (see Sect. 3.1) instead. Nevertheless, AIMD simulations can still be performed for the electrode materials for other purposes, e.g., to estimate the diffusion pathways of the alkali ions, site occupancy, etc.

As a final note for AIMD simulations, the ionic diffusivity (and activation energy) of a material at ambient temperatures is essentially obtained via linear extrapolation from those obtained at elevated temperatures. This implies that the diffusion mechanisms between the ambient temperatures and elevated temperatures must stay unchanged. For materials where such condition does not hold, the NEB method should be utilized instead.

4 Conclusion and Outlook

This chapter provides a general overview of the well-established first-principles methods used in battery-related studies (electrodes, electrolytes, and their interfaces) from both the thermodynamic and kinetics aspects. These include many key properties of alkali-ion battery: equilibrium voltage, phase stability, electronic structures, and ionic diffusion properties. First-principles calculations need to have closed-loop interaction with experimental design and data. Simulations provide insight into development of new materials and aid in the interpretation of experimental observations. Experimental results in turn prove the validity of the theoretical model and proposed mechanism. Despite the remarkable advances of the first-principles methods in recent years, there remain some pressing challenges in modeling technique when it comes to (1) noncrystalline systems, e.g., the presence of intrinsic defects and the electrolyte/electrode interfaces, and (2) the design of high-voltage high-capacity cathode materials.

First, it should be noted that most of the first-principles methods presented here, e.g., voltage calculations and NEB methods, have mainly been applied to perfect crystalline solids. From the experimental perspective, however, intrinsic defects such as dislocations, stacking fault, and micro-strain are always present in the synthesized material. These intrinsic defects can have significant impact on the electrochemical performance of the battery material. In principle, imperfections (e.g., dopants) can be modeled via the construction of supercell, and the size of the supercell depends mainly on the defect concentration. Given that there are often more than one possible configuration upon the introduction of defects, an efficient structural enumeration is needed to be performed, which is followed by DFT calculations for each possible distinct configuration. Hence, it eventually leads

to the lowest-energy doped structure. This procedure is often computationally very expensive, especially in the dilute defect concentration.

Solid electrolyte/electrode interface is another important example of noncrystalline first-principles modeling, which is highly challenging at the current stage. To obtain realistic results, the required supercell needs to be sufficiently large, especially the length along the normal of the interface that aims to minimize the artificial interactions between periodic images. In principle, the AIMD method is suitable for interfacial diffusion studies at finite temperatures. Nevertheless, the required long simulation time scales as well as the length scales indicates that such simulations are almost computationally infeasible.

For cathode materials, it should be noted that this chapter is mainly devoted to intercalation electrode materials, wherein energy storage is possible through a reversible intercalation in a stable host framework. Although anionic redox has been recently discovered and confirmed, the capacity of this intercalation type electrode material is mainly limited to one electron per transition metal. Conversion and alloy reactions in electrode material are thus proposed to achieve higher capacities. More oxidation states of TM are feasible in conversion and alloy-type electrodes, which allows more electrons to reversibly change during electrochemical cycling. Similar to intercalation reactions, the thermodynamics of conversion/alloy reactions can be investigated from first-principles calculations by computing the total energy of all the involved compounds. Additional complexity does exist since conversion/alloy reactions produce multiple phases or domains with different chemical composition, where interface and nanosize effects (i.e., requiring noncrystalline modeling) often dominate the thermodynamic properties of materials.

The solutions to the aforementioned limitations and challenges are multifold. First, computational power will continue to grow rapidly, which can allow for longer simulations and larger system sizes and chemical complexity. Second, multi-scale approaches that aim at bridging the multiple time and length scales are expected to further improve in the future. That enables us to probe even more realistic models with higher computational accuracy. Third, the continued development of automation software tools will also facilitate the studies of battery materials and significantly minimize the researchers' time to monitor the simulations. Fourth, building open-access materials science databases from standardized first-principles high-throughput calculations can also facilitate the first-principles modeling. More importantly, with the rapid increase of the computation data, machine learning models can be trained with a higher prediction power, enabling researchers to discover hidden design rules for battery materials.

References

Anisimov VI, Zaanen J, Andersen OK (1991) Band theory and Mott insulators: Hubbard *U* instead of Stoner *I*. Phys Rev B 44:943–954. https://doi.org/10.1103/PhysRevB.44.943

Anisimov VI, Solovyev IV, Korotin MA et al (1993) Density-functional theory and NiO photoemission spectra. Phys Rev B 48:16929–16934. https://doi.org/10.1103/PhysRevB.48.16929

Aydinol MK, Kohan AF, Ceder G et al (1997) Ab initio study of lithium intercalation in metal oxides and metal dichalcogenides. Phys Rev B 56:1354–1365

Bron P, Johansson S, Zick K et al (2013) Li10SnP2S12 – an affordable lithium superionic conductor. J Am Chem Soc 135:15694–15697. https://doi.org/10.1021/ja407393y

Bruno M (2013) The reconstruction of dipolar surfaces: a preliminary step for adsorption modeling. Cryst Res Technol 48:811–818. https://doi.org/10.1002/crat.201200707

Car R, Parrinello M (1985) Unified approach for molecular dynamics and density-functional theory. Phys Rev Lett 55:2471–2474. https://doi.org/10.1103/PhysRevLett.55.2471

Chevrier VL, Ong SP, Armiento R et al (2010) Hybrid density functional calculations of redox potentials and formation energies of transition metal compounds. Phys Rev B 82:75122. https://doi.org/10.1103/PhysRevB.82.075122

Cococcioni M, de Gironcoli S (2005) Linear response approach to the calculation of the effective interaction parameters in the LDA + U method. Phys Rev B 71:35105. https://doi.org/10.1103/PhysRevB.71.035105

Deng Z, Mo Y, Ong SP (2016) Computational studies of solid-state alkali conduction in rechargeable alkali-ion batteries. NPG Asia Mater 8:e254. https://doi.org/10.1038/am.2016.7

Grimaud A, Hong W, Grimaud A, Hong WT, Shao-Horn Y, Tarascon J-M (2016) Anionic redox processes for electrochemical devices. Nat Mater 15:121–126. https://doi.org/10.1038/nmat4551

Haruyama J, Sodeyama K, Han L et al (2014) Space-charge layer effect at interface between oxide cathode and sulfide electrolyte in all-solid-state lithium-ion battery. Chem Mater 26:4248–4255. https://doi.org/10.1021/cm5016959

Heyd J, Scuseria GE (2004) Efficient hybrid density functional calculations in solids: assessment of the Heyd–Scuseria–Ernzerhof screened Coulomb hybrid functional. J Chem Phys 121:1187. https://doi.org/10.1063/1.1760074

Heyd J, Scuseria GE, Ernzerhof M (2003) Hybrid functionals based on a screened Coulomb potential. J Chem Phys 118:8207. https://doi.org/10.1063/1.1564060

Heyd J, Scuseria GE, Ernzerhof M (2006) Erratum: "Hybrid functionals based on a screened Coulomb potential" [J. Chem. Phys. 118, 8207 (2003)]. J Chem Phys 124:219906. https://doi.org/10.1063/1.2204597

Hohenberg P, Kohn W (1964) Inhomogeneous electron gas. Phys Rev 136:B864. https://doi.org/10.1103/PhysRevB.7.1912

Hutter J (2012) Car-Parrinello molecular dynamics. Wiley Interdiscip Rev Comput Mol Sci 2:604–612. https://doi.org/10.1002/wcms.90

Jain A, Ong SP, Hautier G et al (2013) Commentary: the materials project: a materials genome approach to accelerating materials innovation. APL Mater 1:11002. https://doi.org/10.1063/1.4812323

Jonsson H, Mills G, Jacobsen KW (1998) Nudged elastic band method for finding minimum energy paths of transitions. In: Classical and quantum dynamics in condensed phase simulations. World Scientific, Singapore, pp 385–404

Kohn W, Sham LJ (1965) Self-consistent equations including exchange and correlation effects. Phys Rev 140:A1133–A1138. https://doi.org/10.1103/PhysRev.140.A1133

Langreth DC, Mehl MJ (1983) Beyond the local-density approximation in calculations of ground-state electronic properties. Phys Rev B 28:1809–1834. https://doi.org/10.1103/PhysRevB.28.1809

Leung K, Budzien J (2010) Ab initio molecular dynamics simulations of the initial stages of solid-electrolyte interphase formation on lithium ion battery graphitic anodes. Phys Chem Chem Phys 12:6583–6586. https://doi.org/10.1039/b925853a

Lewis NS (2007) Powering the Planet. MRS Bull 32:808–820. https://doi.org/10.1557/mrs2007.168

Marx D, Parrinello M (1996) Ab initio path integral molecular dynamics: basic ideas. J Chem Phys 104:4077. https://doi.org/10.1063/1.471221

Meng YS, Arroyo-de Dompablo ME (2009) First principles computational materials design for energy storage materials in lithium ion batteries. Energy Environ Sci 2:589. https://doi.org/10.1039/b901825e

Morgan BJ, Madden PA (2014) Relationships between atomic diffusion mechanisms and ensemble transport coefficients in crystalline polymorphs. Phys Rev Lett 112:145901. https://doi.org/10.1103/PhysRevLett.112.145901

Murch G (1982) The haven ratio in fast ionic conductors. Solid State Ionics 7:177–198. https://doi.org/10.1016/0167-2738(82)90050-9

Okubo M, Yamada A (2017) Molecular orbital principles of oxygen-redox battery electrodes. ACS Appl Mater Interfaces 9:36463–36472. https://doi.org/10.1021/acsami.7b09835

Ong SP, Wang L, Kang B, Ceder G (2008) Li-Fe-P-O_2 phase diagram from first principles calculations. Chem Mater 20:1798–1807. https://doi.org/10.1021/cm702327g

Ong SP, Chevrier VL, Hautier G et al (2011) Voltage, stability and diffusion barrier differences between sodium-ion and lithium-ion intercalation materials. Energy Environ Sci 4:3680. https://doi.org/10.1039/c1ee01782a

Richards WD, Miara LJ, Wang Y et al (2016) Interface stability in solid-state batteries. Chem Mater 28:266–273. https://doi.org/10.1021/acs.chemmater.5b04082

Roy P, Srivastava SK (2015) Nanostructured anode materials for lithium ion batteries. J Mater Chem A 3:2454–2484. https://doi.org/10.1039/C4TA04980B

Shin D, Saal J (2018) Computational materials system design. Springer, Cham

Sun W, Dacek ST, Ong SP et al (2016) The thermodynamic scale of inorganic crystalline metastability. Sci Adv 2:e1600225–e1600225. https://doi.org/10.1126/sciadv.1600225

Tang H, Deng Z, Lin Z et al (2018) Probing solid–solid interfacial reactions in all-solid-state sodium-ion batteries with first-principles calculations. Chem Mater 30:163–173. https://doi.org/10.1021/acs.chemmater.7b04096

Tarascon J-M, Armand M (2001) Issues and challenges facing rechargeable lithium batteries. Nature 414:359–367. https://doi.org/10.1038/35104644

Tasker PW (1979) The stability of ionic crystal surfaces. J Phys C Solid State Phys 12:4977–4984. https://doi.org/10.1088/0022-3719/12/22/036

Urban A, Seo D-H, Ceder G (2016) Computational understanding of Li-ion batteries. npj Comput Mater 2:16002. https://doi.org/10.1038/npjcompumats.2016.2

Wang L, Zhou F, Meng YS, Ceder G (2007) First-principles study of surface properties of Li Fe P O_4: surface energy, structure, Wulff shape, and surface redox potential. Phys Rev B 76:165435. https://doi.org/10.1103/PhysRevB.76.165435

Wolverton C, Zunger A (1998) First-principles prediction of vacancy order-disorder and intercalation battery voltages in Li_xCoO_2. Phys Rev Lett 81:606–609. https://doi.org/10.1103/PhysRevLett.81.606

Zhou F, Cococcioni M, Marianetti CA et al (2004) First-principles prediction of redox potentials in transition-metal compounds with LDA + U. Phys Rev B 70:235121. https://doi.org/10.1103/PhysRevB.70.235121

Zhu Y, He X, Mo Y (2015a) Origin of outstanding stability in the lithium solid electrolyte materials: insights from thermodynamic analyses based on first-principles calculations. ACS Appl Mater Interfaces 7:23685–23693. https://doi.org/10.1021/acsami.5b07517

Zhu Z, Chu I-H, Deng Z, Ong SP (2015b) Role of Na + interstitials and dopants in enhancing the Na + conductivity of the cubic Na 3 PS 4 superionic conductor. Chem Mater 27:8318–8325. https://doi.org/10.1021/acs.chemmater.5b03656